machines

MDPI

Article

Experimental Investigation of Two Switching States of an Active Foil Bearing during Start-Up

Hannes Schmiedeke [1,*], Jan-Hinrich Sick [2] and Michael Sinapius [1]

[1] Institute of Mechanics and Adaptronics, TU Braunschweig, 38106 Braunschweig, Germany; m.sinapius@tu-braunschweig.de
[2] SBS Sondermaschinen GmbH, 38104 Braunschweig, Germany; jan-hinrich.sick@sbs-sondermaschinen.de
* Correspondence: h.schmiedeke@tu-bs.de

Abstract: The next few years will be marked by major changes in the mobility sector in order to come closer to CO_2 neutrality. Especially in the commercial vehicle sector, fuel cells can make an important contribution. In order to achieve this, the efficiency of all subcomponents of a vehicle has to be improved. This also includes the bearings in the electrical air compressors. The frequent start–stop cycles are critical, as they can lead to higher wear and thus a shorter service life. One solution is a prototype that can actively switch between a triangular profile and a round bearing shape. In this work, the two switching states are investigated experimentally. Instead of the thin bearing sleeve of the prototype, rigid sleeves are used for each switching shape. This allows the shape itself to be studied without the contribution of the stiffness of the thin bearing sleeve along with the actuators. The examination includes static load tests and run-out tests in the range of the lift-off speed. Alongside this, the difficulties of the bearing production and the improvement of the test rig used are pointed out.

Keywords: active foil bearing; bump-type; drag torque; lift-off speed; bearing stiffness; foil manufacturing; test rig

Citation: Schmiedeke, H.; Sick, J.-H.; Sinapius, M. Experimental Investigation of Two Switching States of an Active Foil Bearing during Start-Up. *Machines* **2022**, *10*, 447. https://doi.org/10.3390/machines10060447

Academic Editor: Davide Astolfi

Received: 21 April 2022
Accepted: 2 June 2022
Published: 6 June 2022

1. Introduction

Talking about climate protection and acting accordingly simultaneously raises the questions of how to reduce the use of fossil raw materials and at the same time make optimal use of the available energy. Of increasing interest, fuel cell vehicles are attractive for commercial vehicles due to their comparatively fast refuelling compared to battery vehicles, their climate-friendly reaction products and their low weights. As with internal combustion engines, the power density is increased by pre-compressing the air before it is fed into the fuel cell. It must be noted that the compressed air must not be contaminated with the lubricant of the bearings in the compressor. The compressors used are characterised by high speeds of about 100,000 rpm and more to achieve high efficiency [1]. Air bearings, especially foil bearings, are a promising solution. They have low-friction, require little installation space and, due to the media lubrication, do not require oils and the necessary peripheral equipment. The bump-type foil bearing has been the subject of many investigations so far. It consists of a rigid bearing sleeve, a wavy spring structure (bump foil) and a smooth top foil. This combination is able to compensate the expansion of the shaft due to the centrifugal force and the temperature. The friction within the foil structure also increases the damping effect needed to overcome self excitation and shocks at high speeds [2]. Agrawal [3] points out that gas bearings were already being used by AirResearch for air cycle machines for planes in the mid-1960s. Some years later, they built a turbo-alternator compressor based on air foil bearings that works well. In those applications, the foil bearings proved to be more advantageous than the roller bearings [3]. In 2000, Heshmat et al. [4] demonstrated the use of foil bearings in a turbo charger. Six years later, they presented a work about using foil bearings in an air compressor for fuel cells [5]. The tests showed low vibrations

and good shock tolerance. The service life of the compressor, on the other hand, was strongly dependent on the wear of the bearing. Especially at low speeds and therefore at every restart, the shaft and the foils rub directly against each other. In addition to wear, the friction also leads to an increased temperature inside the bearing. In some applications, such as turbochargers, turbines or Auxiliary Power Units [3], the ambient temperature around the bearings is already elevated. Overall, this causes thermal stress on the materials and could increase the wear [3].

The examination of the foil bearings as individual components is therefore very important in order to be able to optimise the service life of the bearings and thus also of the compressors. In the literature, two common concepts are used. For rotordynamic investigations, a shaft is inserted into two bearings and accelerated up to a desired speed. Typically, the orbits are recorded and searched for the occurrence of sub-frequency vibrations. The latter can lead to bearing failure due to the low damping at high speeds. The other concept used in this work is based on a rigidly mounted shaft. The bearing floats on the shaft and can deflect radially according to the pressure build-up in the smallest gap. The advantages are that only one test bearing is required, the bearing can be loaded as desired and the frictional torque can be recorded easily [6]. DellaCorte [7] examined on a test rig with floating bearing the effect of temperature on the operating behaviour up to 70,000 rpm and 650 °C. The test rig consists of an engine on whose shaft the test bearing (generation I; inner diameter: ø 35 mm) is mounted. The sleeve of the bearing is secured against rotation with a torque arm. Similar to the enhanced test rig in Figure 1, there is also a pneumatically actuated loading device on the sleeve. The temperature is controlled via heating rods next to the bearing. The tests show that the bearing used also functioned at 650 °C or with a load of 250 N. Nevertheless, higher temperatures resulted in lower load capacities and higher loads resulted in higher frictional torques. In contrast, Howard [8] picked up on the first concept. Here the shaft is driven by a compressed air turbine and held in two test bearings. Monitored by inductance type displacement sensors, the influence of the bearing on the rotor dynamics could be investigated. The novelty is that each of these test specimens is mounted in roller bearings to achieve a rigid but rotatable support. This allows the use of an arm to measure the frictional torque at each time step. A combination of the ideas of both test rigs can be found in the publication by Rudloff et al. [9] as well as in Figure 1. Although they refer to the work of Ertas [10], their mounting of the test bearing is closer to the design of Howard [8]. The supposed advantage is that the force application does not generate any torque due to misalignment. The shaft itself is supported by rigid ceramic ball bearings and can be accelerated by an engine up to 40,000 rpm. The publication also shows, using a simple bump type bearing (generation I; inner diameter: ø 31.8 mm) as an example, that the lift-off speed increases with increasing load from approx. 3000 rpm (10 N) to approx. 4500 rpm (50 N). Similarly, the breakaway torque increases from approx. 0.07 Nm (10 N) to approx. 0.28 Nm (50 N). Rudloff et al. also show the stiffness and the damping in a study of the dynamic properties, but point out that the linearised behaviour in the evaluation cannot adequately reflect the non-linear behaviour of the bearing.

Based on these and other investigations, the bearings have been continuously improved to run stable on even higher speeds by adjusting the dynamic properties' damping and stiffness. The bump foils were segmented to obtain different axial, circumferential or radial stiffnesses (generations II and III) [2]. Some research institutions have also been working on alternative spring elements. San Andrés et al. [11] compare a simple bump type bearing (generation I, inner diameter: ø 36.61 mm) with a metal mesh type bearing. Static tests show a slightly greater damping of the metal mesh structure. The operating behaviour is shown on a test rig that is very similar to the concepts by DellaCorte [7] and Ertas [10]. Unlike Rudloff et al. [9], the bump type bearing only lifts off at approx. 30,000 rpm. This is about 5000 rpm greater than the metal mesh type bearing. Both bearings show an increase in frictional torque and a shift to higher lift-off speeds with increasing load. In a later work [12], San Andrés et al. mounted shims below the bump foils to increase the mechanical preload of the bearing (resulting in generation II, inner diameter: ø 37.98 mm).

This adjustment not only leads to small change in stiffness during operation, but also to an apparent increase in direct damping. Interestingly, the bearing with 30 µm shims has better lift-off behaviour than without any or with 50 µm shims. Sim et al. [13] also use 30 µm thick shims in a bearing originally assigned to generation I (inner diameter: ø 25.4 mm) to improve the running characteristics in a turbocharger. In fact, the sub-synchronous oscillations only occur at higher speeds and with significantly smaller amplitudes. The geometric change due to the thickness and the position of the shims is shown very clearly by means of static load curves. The frictional torque is not examined. A further study of the research group [14] with lobed sleeves instead of shims confirms the relation between preload, the dynamic coefficients (stiffness, damping) and thus the onset speed of instability of the bearing (generation II, inner diameter: ø 40.3 mm). Mahner et al. [15] consider another circumstance that can increase the preload in the bearing (generation II, shaft diameter: ø 30 mm). They use foils that have about twice the radius of curvature compared to the nominal bearing radius. The mounted foils therefore press against the shaft despite the clearance. Measurements on a test rig similar to [7] show an increase in friction torque for the bearing with the bigger top foil radius also with increasing static loads. On the other hand, the bearing with the greater preload seems to lift off sooner. The increase in lift-off speed with increasing load is again in line with the literature mentioned above.

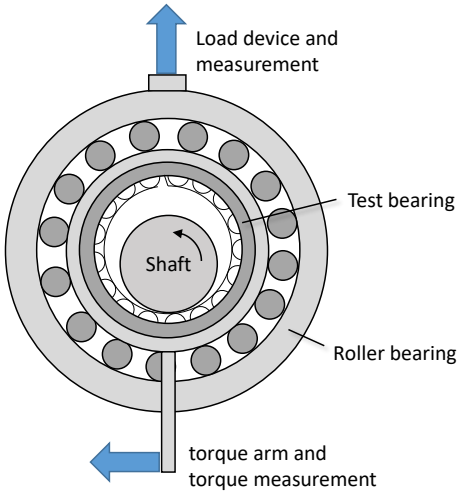

Figure 1. Enhanced design of a test rig for the start-up measurements according to [9].

In summary, the improvements in the stability of the bearings allow one to operate them safely at even higher speeds and therefore they contribute to an increased performance of their surrounding systems. Air compressors can be smaller and thus lighter for the same performance [1]. On the other hand, these improvements often lead to a higher lift-off speed and so to more power loss, increased heating and more wear [16]. Coatings such as PTFE (used by Mahner et al. [15]) or MoS_2 (used by Sim et al. [14]) as well as a texturing of the surface [17] reduce the symptoms, but cannot eliminate the problem. Especially in mobile applications, systems are often switched off and thus frequently pass through the area of mixed friction. A combination of aerostatics in the start-up area and aerodynamics in the operating area seems to be a logical consequence. Kim et al. [16] demonstrate this on a bump-type bearing (generation III, inner diameter: ø 101.6 mm). The initial friction is significantly lower than that of comparable bearings and the temperature in the bearing also decreases with the increase in feed pressure. Another approach is to actively modify the housing to adjust both the bearing clearance and the preload. A round shape (without preload) results in low friction and early lift-off in the starting range, while a triangular shape contributes to greater damping at high speeds. Ha et al. [18] describe a sleeve with several elastic hinges and six piezo stack actuators which can lift the shaft due to vibration and the resulting squeeze films, as well as maintain a static circular or triangular profile

shape. Feng et al. [19] use a similar idea, but avoid the complex sleeve with the hinges. Their bearing (seemingly generation I, shaft diameter: ø 30 mm) has a lever below each of the three segments, which is pressed under the bump foil via piezo stack actuators. The geometric influence is similar to that of shims up to a thickness of 70 µm. As expected, the tests therefore show an increase in the frictional torque and the lift-off speed. Further investigations of the same group show that this approach is able to decrease the amplitudes of subsynchronous vibrations [20]. The best actuation parameters for each speed are set by a PID controller [21]. Park et al. [22] locate the piezo actuators directly below the bump foil. A lever is not required. Depending on how many of the nine circumferentially positioned actuators are switched on, a uniform change in clearance or a local preload can be adjusted. Rotordynamics simulation shows the improvement of the proposed design. The use of an active top foil is considerably more demanding. Sytin et al. [23] present a thrust bearing with multi-layer running foils. The foil consists of a stable base layer, a piezoelectric layer and a wear protection layer. By applying voltage, the natural vibration behaviour of the bearing can be influenced. A significantly different implementation is discussed by Sadri et al. [24]. Instead of the stiff stack actuators mentioned above, the thickness of the sleeve is reduced to 0.25 mm and covered with piezo patch actuators. This structure is much more adaptable and has additional damping potential due to the piezoelectric effect. Sadri et al. note that the contribution of the actuators to the stiffness of the bearing was insufficiently taken into account in the previous publications about active bearings. Simulations and first prototypes demonstrate the general properties. This work is therefore intended as an important milestone to show how the two switching states behave without any change in stiffness due to the actuators and the thickness of the sleeve in the start-up range. For this purpose, this work shows the investigation of two different sleeves (see Figure 2). Both shapes differ in preload (round: 0 µm; triangular profile: 397 µm) as well as in radial bearing clearance (round: 100 µm; triangular profile: 30 µm) adopted from [25]. The stiffness of both bearing rings is nearly the same. Just like in the active prototype from Sadri et al. [25], the same foils are used for both bearings in order to keep the manufacturing deviations low. In addition, this work presents an enhanced test rig in order to be able to carry out more extensive and more precise measurements in accordance with Sadri's hypothesis. The most important measured value is the friction torque. This can be used to estimate the energy requirement, the heating in the bearing and the lift-off speed. In combination, these results describe the starting behaviour of the two switching states. The difference shows the potential of Sadri's prototype. This work is supplemented by displacement measurements during the investigation with a non-rotating shaft as well as during all start-up tests to calculate the actual bearing clearance as well as the stiffness of the bearing. The first is strongly dependent on manufacturing deviations and is primarily used to check the extent to which the two bearings in this study can be compared with Sadri's simulations. The stiffness is used to show how much the shape can adjust the compliancy of the bearing. In addition to the prediction of the rigid body modes, this is important for further work that evaluates the contribution of the actuators.

2. Materials and Methods

2.1. Test Bearing

The bearing sleeve of Sadri et al. [24] is made of 1.4301 and is wire-eroded. In order to obtain the same material and contact properties with the foil structure, the sleeves in this work have been manufactured in the same way and on the same machines. Type A corresponds to an ideal round shape with inner diameter ø 39.4 mm. Type B (triangular profile) is composed of three off-centre circles that lead to 120° segments, as visible in Figure 2a. The exact dimensions can be found in Table 1.

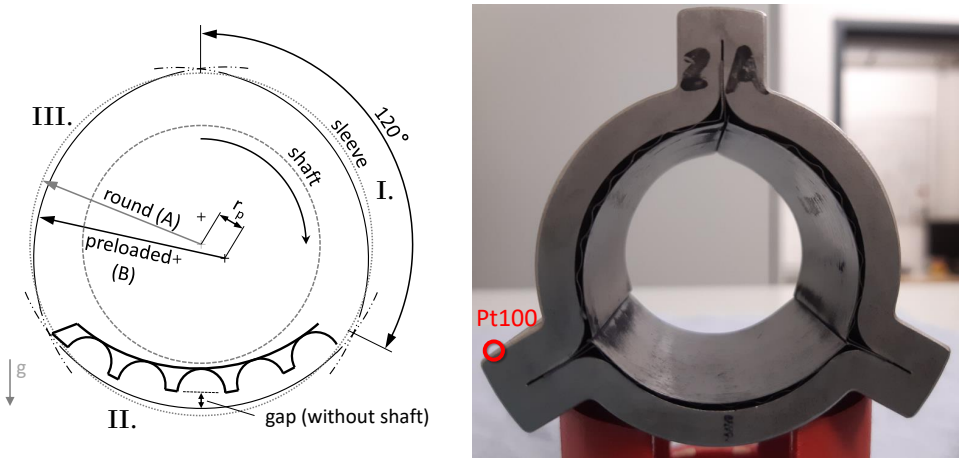

(**a**) (**b**)

Figure 2. The test bearing used in this study. (**a**) Draft of the two shapes with roman numerals to distinguish the segments; (**b**) bearing with sleeve type A after the first measuring series and with the location of the Pt100 temperature sensor.

Table 1. Nominal and measured (*) parameters of the used bearings.

Parameter	Symbol	Value	Unit
bearing width	b	40	mm
shaft diameter	d_s	37.8	mm
segments	n_s	3	-
sleeve radius	r_{round}	19.7	mm
	$r_{preloaded}$	20.048	mm
	r_{outer}	25	mm
sleeve preload	r_p	418	µm
bumps per foil	n_b	7	-
bump height	h_b	500 (≈489 *)	µm
bump half-length	l_b	1.81	mm
bump distance	So_b	4.59 (≈4.60 *)	mm
foil thickness	t	0.1	mm
material sleeve		1.4301	-
material shaft		1.4057	-
material foils		1.4310	-
material coating		MoS_2	-

The foil structure is created following the manufacturing process by Della Corte et al. [26]. They use pre-cut sheets of annealed Inconel X-750. The raw sheet is placed on a die with round grooves and covered with a rubber plate. Finally, a metal plate is placed on top of the rubber plate to distribute the forces of the press evenly. The final step is a heat treatment. For this work, a cold-rolled spring steel (1.4310; 0.1 mm thick) is used. It was already work-hardened in raw state and thus required some adjustments to the procedure. It has been shown that with bump heights of more than approx. 400 µm, the foil is always torn in the area of the sharpest bends (between the bumps), even with rounded edges (radius: 0.25 mm). As an alternative to forming with high temperature as performed by Shalash et al. [27], the use of a separating foil (80 µm thin; polyolefin-copolymer) between the die and the blank helped to achieve greater bump heights and to keep sharp edges. Furthermore, a PTFE plate is used instead of the rubber plate. Before pressing, the foils are bent on one side in order to be able to fix them later in the sleeve. A final heat treatment was not carried out. The foils were only carefully recurved by a thin rod (ø 18 mm), as the pressing had already resulted in a main curvature of approx.

20 mm (radial). The top foils consist of the same blanks and are bent to the target curvature in a round bending machine. The latter was specially designed for the high springback of the foil material. To avoid fretting, the top foil was coated with MoS_2 (OKS 521). The additional thickness of the top foil was compensated by a slight reduction in bump heights (see Table 1). This was achieved through lower pressing forces (approx. 140 kN). As the results of 22 bump foils in Figure 3 show, the production of bump foils involves considerable dimensional uncertainty. Shalash et al. [27] came to a similar conclusion. Their hot forming process with two dies resulted in an error of up to 24% of the bump radius. In fact, there are now improved processes that achieve better reproducibility by means of a rolling movement of the punches. With the use of modern 3D printers, as shown by Zywica et al. [28], the dies can be adapted quickly and produced cost-effectively. However, this procedure was not used for this work, as the dies used had already been produced and tested before Zywica's publication appeared. Since the same foils are used in both bearings, the influence of the production deviations is estimated to be low. The active prototype of Sadri [25] also uses just one set of foils. Due to the production quantity, three very similar foils with a height of approx. 490 µm could be selected.

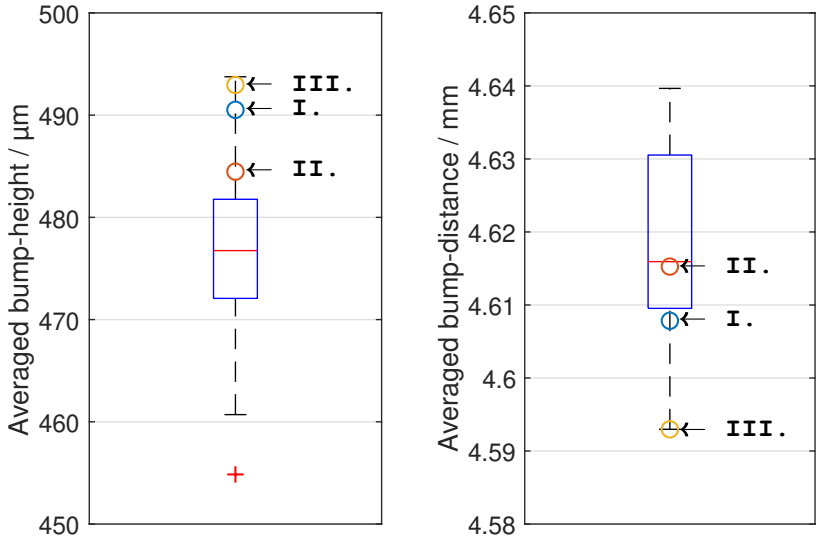

Figure 3. Bump heights and bump distances with median (red line), the range from the 25th to the 75th percentile (box), the range from the minimum to the maximum (dashed line) and the statistical outlier (red cross).

The foils are measured using a profile scanner (scanCONTROL 2910-50; MICRO-EPSILON MESSTECHNIK GmbH). A Matlab program is used to estimate the principal curvature based on the measured values and thus also to determine the bump heights (see Figure 4). The evaluation also shows that the manufacturing process described above does not produce perfectly round shapes. The curvature is stronger in the middle of the foil than at the ends. The authors therefore use polynomials. Up to and including the third degree, the circular approximations are better. From the fourth degree (used here), the polynomials represent the contour better. However, the larger the degree, the wavier the approximation becomes, which results in a distortion of the calculated bump heights. At the ends of the foil, the fitted polynomials show strong changes in curvature that do not visually fit the shape of the foil. Although the polynomial is slightly different for each foil, it can be seen visually with comparable intensity, as in the sketch in Figure 4. For the evaluation, therefore, only the middle four bumps were included in the mean value in Figure 3 and the averaged mean value in Table 1. Even though the absolute value is quite uncertain, the foils can still be compared with each other. However, with regard to the stiffness measurements in Section 3, the values seem to be plausible.

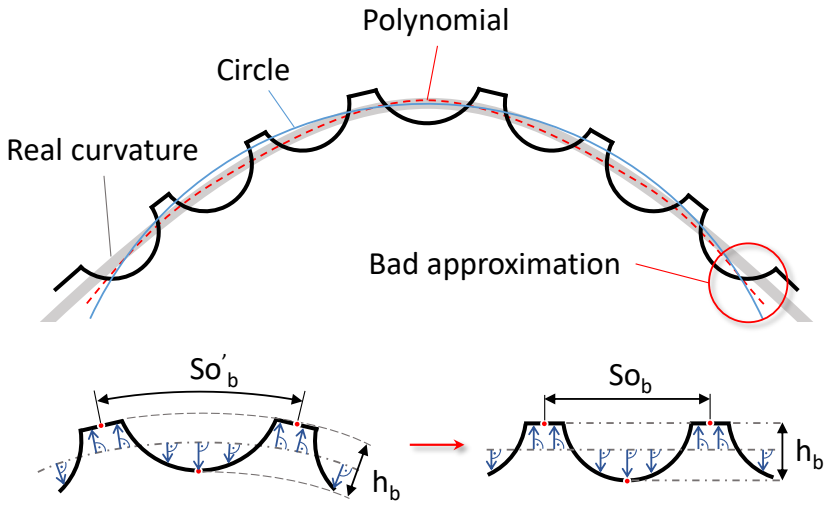

Figure 4. Bump dimension identification procedure: The shapes of the foils are not circular and are therefore generalised by polynomials. These polynomials together with their perpendicular straight lines (blue arrows) form the bases for the curved coordinate systems (bottom left). With the transformation into Cartesian coordinate systems (bottom right), the foils are virtually decurved and thus an estimation of the bump heights and distances is possible.

2.2. Test Rig

Figure 5 shows the test rig used to compare both bearings. The basic idea is based on the approaches presented above. The bearing floats on the shaft and can be operated by an electric motor up to a speed of 30,000 rpm. Instead of a roller bearing used by Ertas [10] and Howard [8], two rockers prevent torques from being transmitted to the bearing along with the load application. Roller bearings have the disadvantage that due to the static friction a residual torque always remains. This either leads to a poorly reproducible offset in the torque measurement or absorbs part of the torque in the bearing. The measurement is therefore falsified. The improvement in this test rig is that fixed body joints (blue circles) are used as far as possible. These are characterised by a zero backlash and low damping. Moreover, the joints are positioned in the main axes of the bearing and allow movement in all degrees of freedom. To prevent excessive swinging of the bearing holder, another rocker is mounted on the back (not visible in Figure 5). The only limitation is via the torque arm at the bottom of the bearing holder. Another special feature is that the test rig can also exert a force on the bearing in the horizontal axis in addition to the vertical axis. In the simplest case, the bearing holder can be ideally aligned centrally to the shaft to compensate assembly error. Static loads or shocks can also be applied. However, the response times of the pneumatic cylinders are significantly shorter than those of shakers used to determine dynamic coefficients. Although the air cylinders are very low friction (graphite piston in a glass tube), they have a static friction force of 1–2% of the actuating force (according to the manufacturer). The weight of the bearing holder (approx. 4 kg) is therefore additionally balanced by a dead weight on the same rocker. Neglecting the inertias, the bearing load is thus nearly independent of the displacement of the bearing holder. The force is measured via strain gauges. Another force sensor is located directly at the torque arm to measure the torque. The measurement of the relative displacement between the test bearing and the shaft is carried out via laser distance sensors. These are mounted in pairs and orthogonally on both bearing sides on the bearing holder. Unlike eddy current sensors, which are often used, laser distance sensors are not sensitive to material inhomogeneities and do not have to be recalibrated for each sample shaft. The bearing holder itself is monitored via an acceleration sensor. Furthermore, the temperatures can be recorded via freely positionable Pt100 sensors and the ambient conditions (temperature, humidity, air pressure) are continuously logged.

The bearings are changed by sliding the entire assembly away from the engine via rails in the axial direction. The shaft is thus disengaged and the separable bearing holder is opened. Depending on the size of the bearing outer ring, the laser distance sensors on one side must be pushed aside slightly. In combination with end stops, a fast and reproducible bearing change is possible. This idea was inspired by the test rig of Nielsen [29].

In summary, this results in a test rig with a high degree of self-adjustment and reproducibility. It is therefore ideal for identifying even the smallest differences between the two bearings presented above.

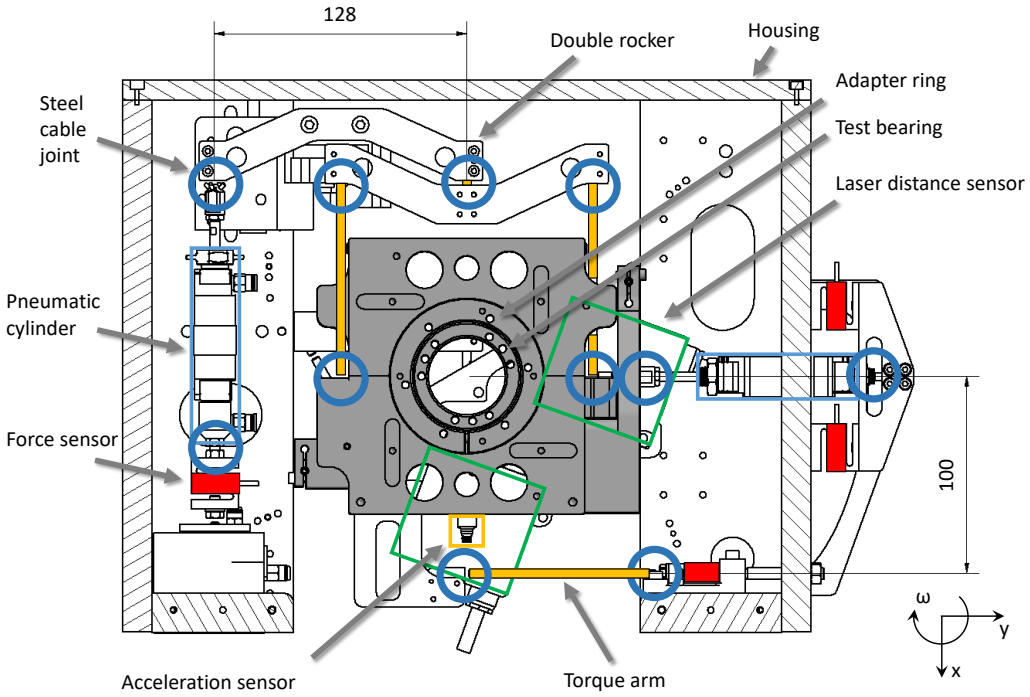

Figure 5. Enhanced lift-off test rig used in this study.

2.3. Test Procedure

In the context of this work, the exact stiffness of the structure is of secondary importance, provided that the structure is identical in all test bearings. More important is the change in stiffness and bearing clearance due to the actuation of the prototype and consequently also between the sleeve shapes presented above. The first results in Section 3 are therefore static load curves. For these measurements, the dead weight is levered out on the test rig so that the weight of the bearing holder presses the shaft against the upper part of the foil structure. Then the pressure in the vertical cylinder is increased and decreased several times (min. ten times) between nearly 0 and approx. 2.7 bar to load the bearing in the opposite direction. The data determined in this way can be found in Figure 6a.

After the static investigations, the results of the start-up tests follow. Each measurement series includes the following preparations to identify all offsets in the measurements:

1. Measurement without the shaft inserted and with the bearing holder aligned over the cylinders to determine the zero point of the vertical and horizontal force.
2. Measurement with shaft inserted and with a higher pressure in the vertical cylinder to adjust the static bearing load.
3. Measurement while the shaft is rotated back and forth alternately and with pauses to determine the static friction torque of the bearing. Assuming that the direction of rotation has no influence on small movements and speeds, the zero point of the torque measurement lies exactly in the middle between the standstill torques, which are measured via the torque arm.

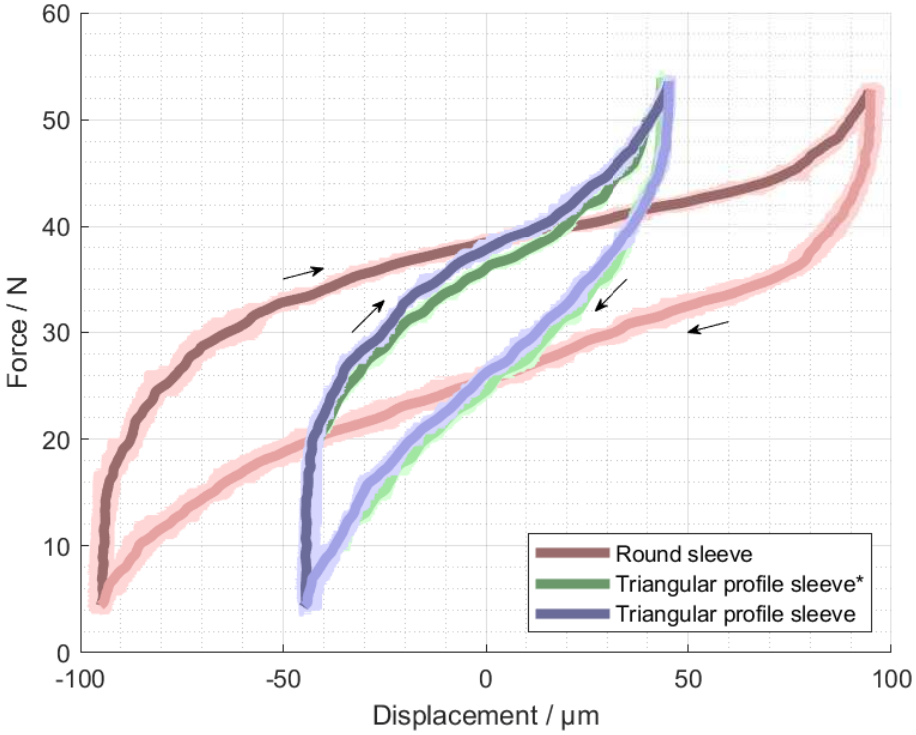

(**a**)

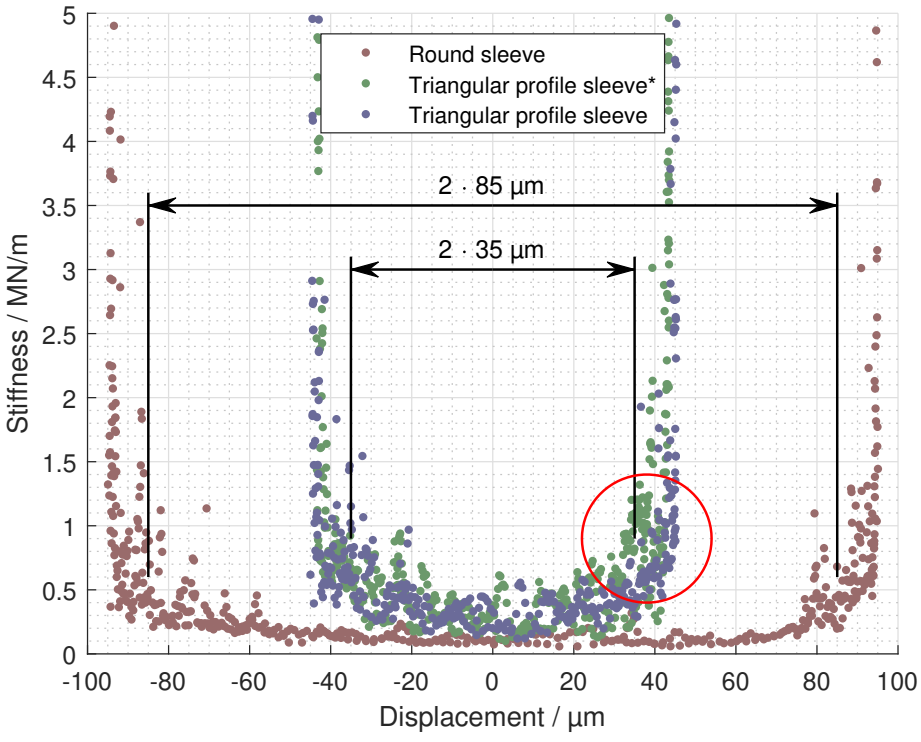

(**b**)

Figure 6. Investigations with non–rotating shaft before (*) and after each measurement series; (**a**) force vs. displacement: the relation of the pronounced hysteresis to the path direction is indicated by arrows. The light shadows behind the averaged curves are the seperated hysterese curves. (**b**) stiffness vs. displacement.

In the next step the motor is started and the shaft is accelerated up to the speed of approx. 16,600 rpm (always the same speed ramp). For stable and smooth operation, the speed is maintained for approx. 1 s before the motor is switched off. The measurement takes place over the entire time, but is only used in the evaluation from this point onwards. Only when the motor is switched off are the external disturbances reduced to a minimum. As soon as the shaft comes to a standstill again, the follow-up measurements begin. Either with identical boundary conditions or with a change in the load. The pressures to generate the loads are set alternately (0.5 bar > 0.7 bar > 0.6 bar; see Figure 7) so that a trend due to increasing temperatures or wear can be assessed later in the evaluation. The range of loads is based on both the publication of Sadri et al. (5 N) [24] and the shaft (1.7 kg; hence approx. 8.3 N per bearing) of the high-speed test rig with which further investigations on the adaptive bearing are planned. Before the actual measurements, three runs at 0.55 bar are also carried out to warm up the bearing and the test stand. Once a bearing has been fully inspected, the shaft is pulled out and the bearing is dismounted to identify possible wear marks and other anomalies. After the components have been photographed (see Figure 8), the sleeve is changed, cleaned and the next series of measurements, including the preparatory steps, begins.

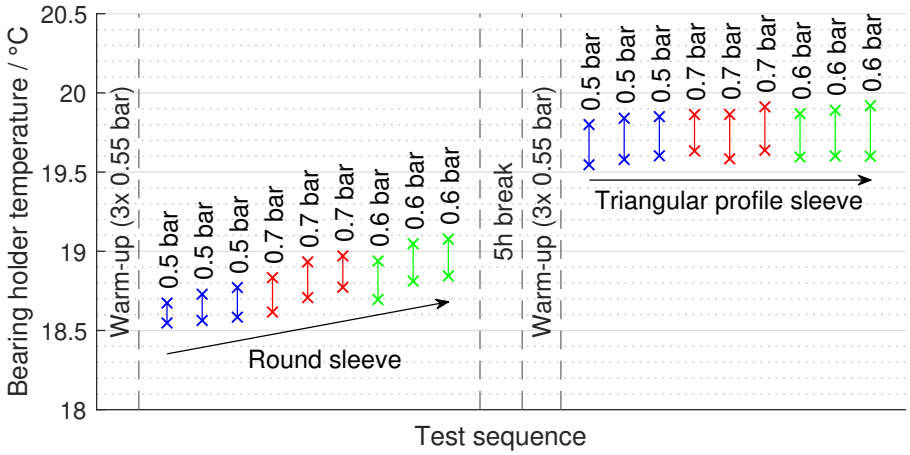

Figure 7. Temperatures and the order of the examinations.

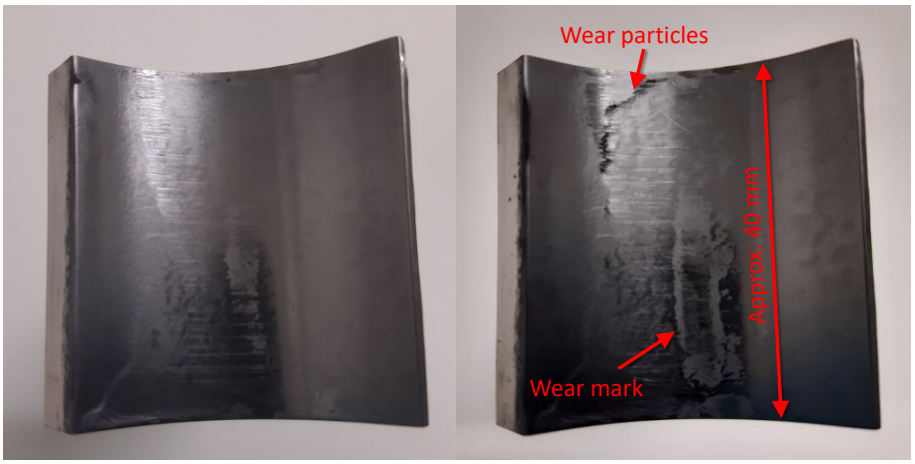

(**a**) I. round (**b**) I. triangular profile

Figure 8. *Cont*.

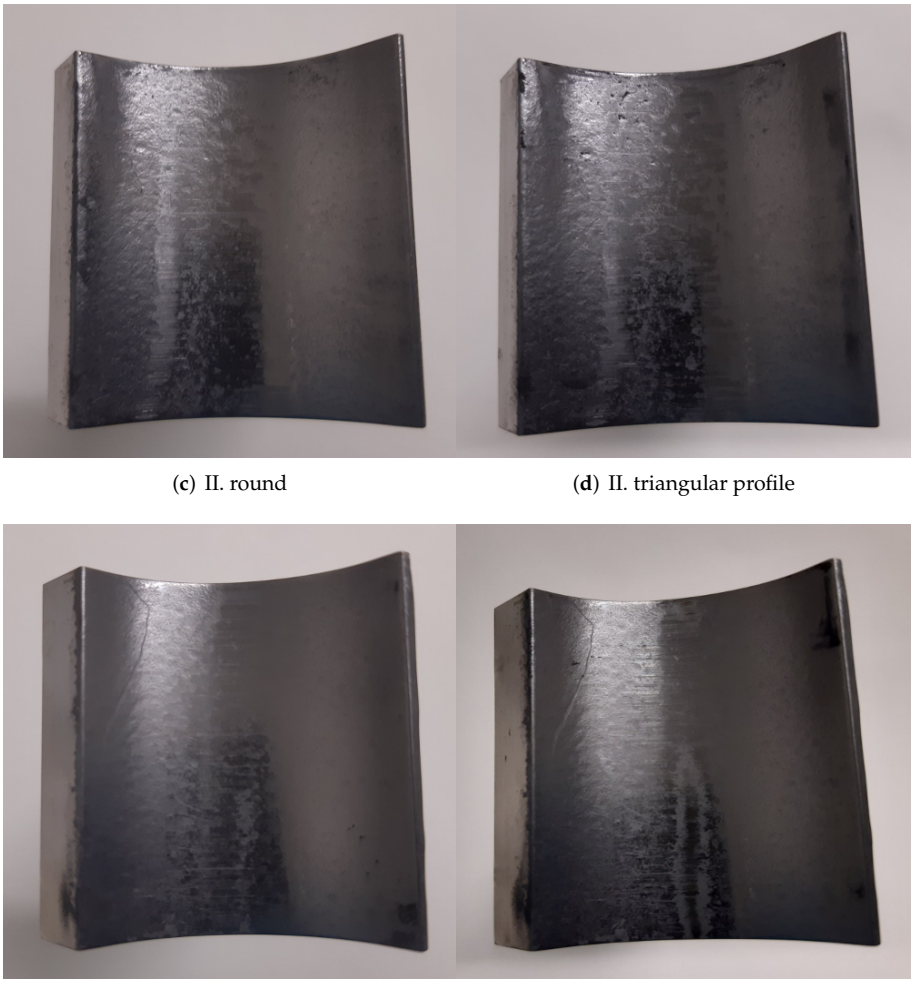

(**c**) II. round (**d**) II. triangular profile

(**e**) III. round (**f**) III. triangular profile

Figure 8. The top foils after the measuring series of both sleeve types (round/cleaned, triangular profile).

3. Results

3.1. Investigations with Non-Rotating Shaft (Standstill)

Figure 6a shows the results of the standstill investigations. The zero point of the force is related to the force in the cylinder and therefore does not equal a zero displacement. Furthermore, the curves are shifted in such a way that the average displacement corresponds to zero. The absolute displacement changes anyway because of a shift of the sensors due to the change of the bearing and is therefore not comparable. The measurement curves themselves were broken down into ten ascending and ten descending curves (shown as shadows) and averaged together (shown as a darker line). The first hysteresis curves are not taken into account, as the foil structure first had to align itself. Even though the static measurements are discussed first, these were in fact carried out after the respective start-up tests. Only the measurement with * corresponds directly to the freshly mounted condition of the triangular profile bearing. The difference between the red-brown (round sleeve) and green (triangular profile sleeve *) hysteresis curves can therefore be attributed to the replacement of the bearing sleeve. Wear cannot have occurred here yet. It can be clearly seen that the curve of the triangular profile shape is more compressed. The bearing has only moved about half as far with the same force. The gradients between the averaged measuring points correspond approximately to the stiffnesses of the respective displacements (Figure 6b). The data points of the round bearing are composed of two areas. The middle (approx. −85 µm to approx. 85 µm) is characterised by a small change

in stiffness between approx. 0.1 and 0.3 MN/m. The outer areas, on the other hand, are characterised by a strong increase in stiffness, which increases tenfold or more within approx. 10 µm. This is contrasted by the triangular profile bearing with an average area of approx. −35 µm to approx. 30 µm before the start-up tests (green curve) and −35 µm to approx. 35 µm afterwards (blue curve). Both curves have a stiffness in the range of approx. 0.2 to 0.9 MN/m. The triangular profile bearing is consequently twice to three times as stiff with small loads below 10 N. The typical curve with the two steep flanks is generally attributed to the increasing contact area between the shaft, the foil structure and the sleeve [15]. In an ideally manufactured bearing according to the specifications of Sadri et al. [24] with a bearing clearance of 100 µm (round) or 30 µm (triangular profile), the middle area would have no stiffness because the shaft would not touch the foil structure at any point within the bearing clearance (with a skew of 0). However, the main curvatures of the foils are not perfectly aligned with the sleeve. Without the shaft inserted, small gaps are visible between all parts as shown in Figure 2. The continuous contact between the foils and the shaft thus leads to an inaccurate determination of the radial bearing clearance. Therefore, the boundaries of the middle areas with approx. 85 µm (round) and approx. 35 µm (triangular profile) are used. When comparing the two hysteresis curves of the triangular profile bearing, it is also noticeable that the bearing clearance has increased on the right side (red circle) by approx. 5 µm due to the start-up tests. The hard stop at approx. 45 µm, however, has remained nearly the same. The authors therefore suspect that this is due to the wear of the foils during operation. Figure 8 shows the top foils after each measurement series. The assembly locations I to III are marked in Figure 2a. The first pictures taken after measuring the round bearing show almost no signs of wear. Only foils I and III show slight grey discolouration in the middle area. This changes with operation in the triangular profile bearing sleeve. The wear marks grow to about half the bearing width and are clearly identifiable. Foil II seems to be a little shinier and some debris has collected in the edge areas (black). If the shaft is only in contact with the wear marks, this would result in a larger clearance. As soon as several bumps are in contact, the proportion of unworn contact surfaces increases. So the stiffnesses before and after the operation converge.

3.2. Lift-Off Tests

Before the tests discussed here were carried out, the rotor was already running in combination with other bearings. During these tests, part of the MoS2 coating settled on the surface of the shaft and lowered the run-out to less than approx. 1 µm (in the center of the running surface). Outside the running surface, the run-out is approx. 2.5 µm. The measurements were taken before the test bearings of this work were installed, which meant that the shaft could be pushed completely into the measuring range of the laser distance sensors without touching the bearing holder itself. The lift-off tests were carried out on one day and at an ambient temperature of 18.5 ± 0.5 °C (first nine measurements) to 19.5 ± 0.5 °C (last nine measurements). Figure 7 shows the temperatures at the sleeves (see Figure 2b). The first nine measurements with the round bearing are characterised by a steady rise in temperature from 18.5 ± 0.5 °C to 18.9 ± 0.5 °C (starting temperature). During a test, the sleeve warmed up by about 0.2 K on average and cooled down again by about the same amount by the time of the next start. About five hours later, the second series of measurements with the triangular profile bearing started with a higher ambient temperature of 19.6 ± 0.5 °C. However, the difference of about 1 K was so small that the influence of the temperature can be neglected. The humidity in the room was always around 40%. Since sealing air was blown into the test chamber of the test rig via the engine, a humidity of about 27% was measured here directly after opening.

Figure 9 shows the friction torques recorded with different loads and using different sleeves. Each curve corresponds to an average of three trials, taking into account all offsets. The two diagrams below show the two bearing sleeves separately and with a logarithmic scale to better visually resolve the transition from mixed friction to fluid friction. As already

described by San Andrés et al. [12], this is characterised by the occurrence of a minimal frictional torque. It can be clearly seen that the frictional torques of the round bearing stabilise at approx. 8500 rpm (load of approx. 4.3 N and approx. 6.2 N). The actual lift-off speed will be slightly higher, but cannot be determined more precisely due to the noisy curve. With the triangular profile bearing, the stabilisation only happens from approx. 10,000 rpm (4.4 N) and approx. 10,500 rpm (6.1 N), i.e., at a speed difference of 1500 rpm to 2000 rpm. A similar difference also exists for loads of 8.2 N. Nevertheless, the behaviour of the three load levels in relation to each other does not seem to be linear. While the start-up phase up to approx. 2000 rpm suggests an even spacing ratio, the friction torque curves with the 0.5 bar and 0.6 bar pressure levels converge much more strongly in the further course and are only approx. 0.001 Nm apart at lift-off. With the round bearing, the curve of 0.7 bar still achieves almost the same frictional torque compared to the lower load when lifting off. In contrast, the friction of the triangular profile bearing is 0.003 Nm to 0.004 Nm greater, even when lifted. Wear cannot be the reason, as the subsequent measurements with 0.6 bar (see the test sequence in Figure 7) do not show such a strong deviation from the results with 0.5 bar. In general, the round bearing seems to have a fluid friction torque that is about 0.007 Nm to 0.008 Nm (0.5 bar and 0.6 bar) and about 0.012 Nm (0.7 bar) lower compared to the triangular profiled one.

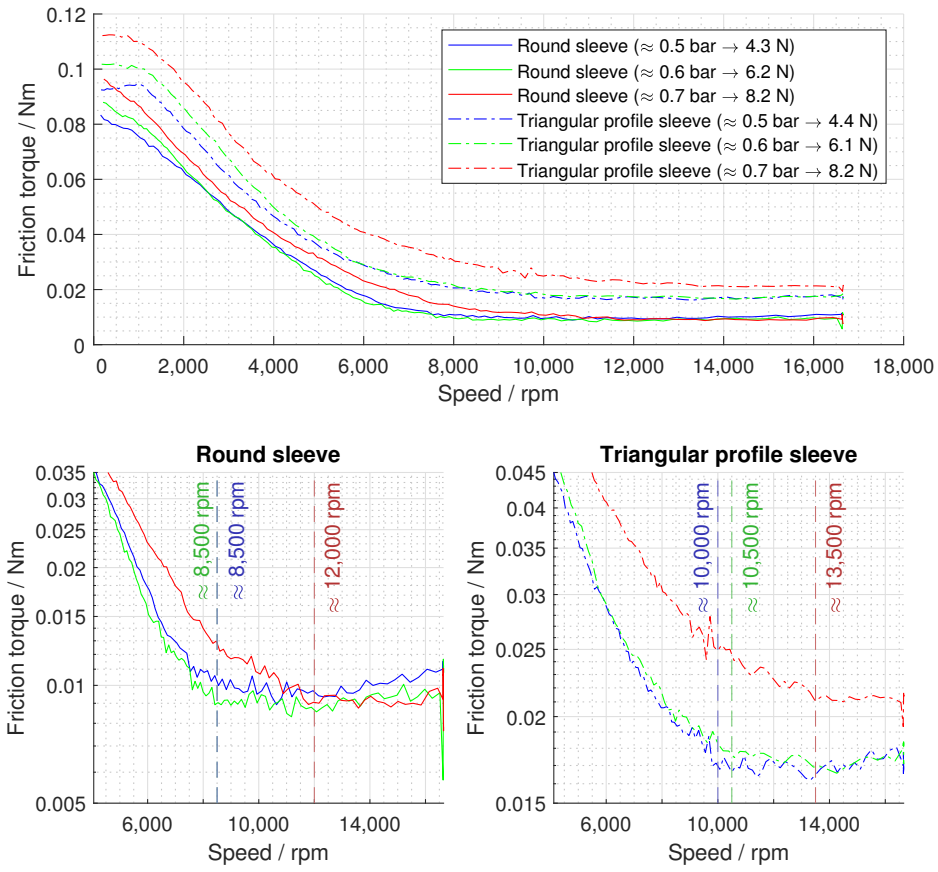

Figure 9. Torque and lift-off during the coast-down tests.

Another difference between the two bearings can be seen in the relative eccentricity between the shaft and the bearing holder (Figure 10). As with the hysteresis curves, the displacement sensors of the same direction are combined in such a way that the movement of the centre of the bearing can be estimated. The zero points correspond to the zero points determined during the static analysis (see Figure 6) and thus correspond approximately to a central position of the shaft in the bearing. Furthermore, the two diagrams are scaled equally. It is thus clearly evident that an increase in load on the triangular profile bearing

leads to a smaller change in eccentricity compared to the round bearing. At standstill, for example the difference of approx. 5.5 µm between the first two load levels (blue and green) is smaller by a factor of approx. 0.36. In addition, the change in eccentricity between standstill and maximal speed is smaller by a factor of 0.4 (blue), 0.41 (green) and 0.54 (red). Figure 11 therefore shows the estimated stiffnesses k_i, which are calculated for each speed (index i) from the measured forces F_i and displacements x_i (Figure 10) of two adjacent curves (blue to green; green to red):

$$k_i = \Delta F_i / \Delta x_i \tag{1}$$

As the static load increases, the absolute difference in stiffness between the bearing with the round sleeve and the bearing with the triangular profile sleeve increases approx. 0.2 MN/m (green) and approx. 0.35 MN/m. The distance remains approximately the same up to the maximum speed.

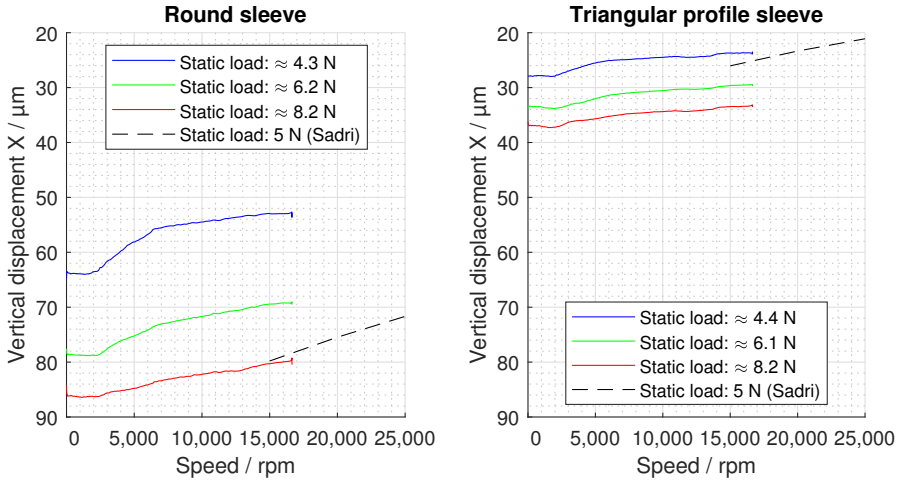

Figure 10. Eccentricities (relative to the centre point of the bearing determined by the tests with non-rotating shaft) and the results of Sadri [25].

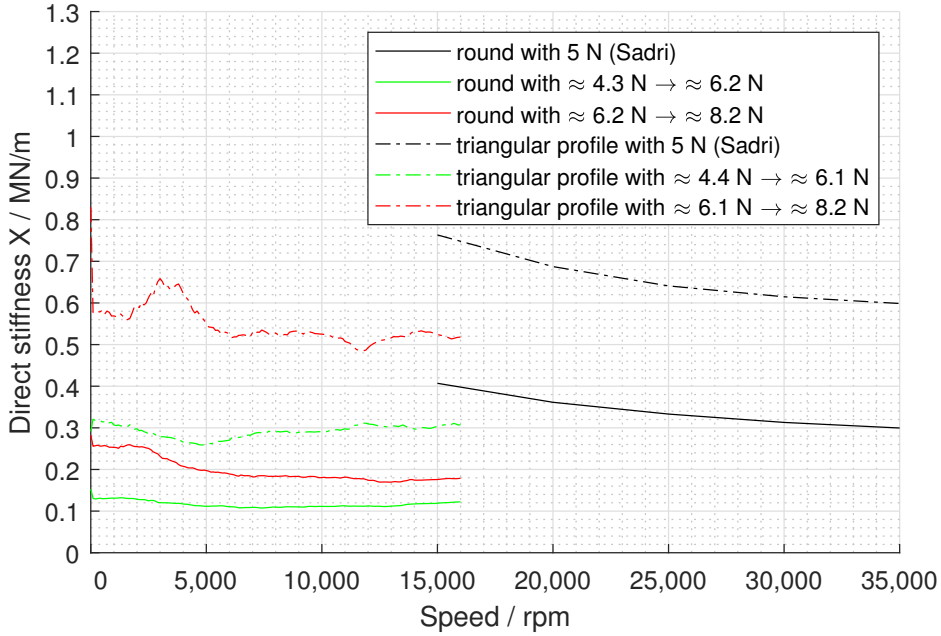

Figure 11. Calculated stiffness from Figure 10 and results of Sadri [25].

4. Discussion

4.1. Comparison with the Literature

In the work of Rudloff et al. [9], the results show an increasing breakaway torque (approx. 0.05 Nm per 10 N) and an increase in lift-off speed (approx. 500 rpm per 10 N) with an increase in load. The lift-off speed is given as approx. 3000 rpm to approx. 5000 rpm. The used bearing is very similar in terms of dimensions (ø 38 mm; 38 mm width; 31.8 µm clearance) compared to the bearing used in this study, but differs in the bearing generation (one circumferential foil pair) and the materials used (e.g., Inconel foils). It is therefore not surprising that the results of the round bearing in Figure 9 also show an increase in the breakaway torque with a similar ratio (round: approx. 0.01 Nm per approx. 2 N). However, the lift-off speed in Figure 9 (8500 rpm to approx. 12,000 rpm) is greater. The change in lift-off speed from approx. 4.3 N to 6.2 N (round) is also very small (hardly distinguishable) and thus similar to Rudloff. In contrast, the change to a static load of 8.2 N ($\Delta F = 2$ N) shows a jump of approx. 3500 rpm. This value is more in line with the observations by San Andrés et al. [12]. Their bearings start to lift off at approx. 20,000 rpm (approx. 5000 rpm per approx. 6500 Pa $\approx$ 9 N). The described bearing dimensions (ø 36.74 mm; 38.1 mm width; 120 µm clearance) are also very similar to the tested bearing in this work. Some of the bearings are mounted with shims (30 µm; 50 µm). In addition to the increase in breakaway torques and lift-off speeds with increasing load, they observed that an increased preload leads to a further increase in breakaway torque of approx. 0.1 Nm (50 µm shims; 0 kPa) and a lift-off speed of approx. 3,000 rpm (50 µm; 0 kPa). The 30 µm shims, on the other hand, cause a reduction in the lift-off speed (approx. 2000 rpm). The latter is given with an uncertainty of $\pm$2500 rpm. In an earlier study of the same researchers [11] with a first generation bearing, friction torques in the lifted state of approx. 0.01 Nm at a static load of 8.9 N were obtained. Interestingly, the next load level with 17.8 N led to the same values, before a jump of approx. 0.01 Nm occurred with 26.7 N. This matches the values of 0.01 Nm to 0.21 Nm in Figure 9. The publications of Rudloff et al. [9] and Mahner et al. [15], on the other hand, cannot be used for a comparison of the absolute values. The friction torque curves show negative areas at the beginning, which indicate an inaccurate offset in the friction torque measurement (see preparation step 3 in Section 2.3, "Test Procedure"). The areas lie with approx. $-$0.025 Nm [9] and approx. $-$0.02 Nm [15] in the range of the actual amount to be expected. The possible error is too large.

In general, the results of the start-up tests of this work seem to be plausible in terms of the magnitude as well as the load and speed dependency. An exact comparison is difficult due to the differences in bearing design. Unlike shims, the prototype by Sadri [25] not only changes the preload but also the bearing clearance. Furthermore, manufacturing errors lead to a greater scatter of the results. Mahner et al. [15] show that even a change in the pre-curvature of the top foil (doubled radius) can lead to a change in the breakaway torques (approx. 0.04 Nm with 5 N static load) as well as the lift-off speeds (increase of approx. 4000 rpm with 5 N static load). As already discussed in the static investigations, the foils used in this work already have a preload in the installed state, even when the bearings are free from external forces. The lift-off speed and the speed differences between the load steps should therefore be higher compared to an ideal bearing.

4.2. Comparison with the Simulation

The goal of this work is to test whether the same differences between the two switching states of the prototype found in simulation can also be observed in experiments. For this reason, the results of Sadri [25] are also shown in Figures 10–12. Firstly, however, it must be pointed out that the bearing clearance of 85 µm (round) and 35 µm (triangular profile) deviates from the simulative assumptions of 100 µm (round) and 30 µm (triangular profile). The round bearing therefore has an approx. 15 µm to 20 µm smaller eccentricity in the experiment (Figure 10). The triangular profile bearing, on the other hand, fits the simulation very well. The dashed curve with a static load of 5 N lies exactly between the curves with 4.4 N and 6.1 N. Instead of the tripling of the eccentricity due to the change

from triangular profile to round, a doubling can still be seen in the experimental results. This difference between the switching states is also visible in the stiffness (Figure 11). In the experiment, the stiffness of the triangular profile bearing at 15,000 rpm is about 0.2 MN/m (green) and about 0.3 MN/m (red) greater than that of the round sleeve. Nevertheless, the stiffnesses at comparable static load (green curve) are approx. 0.3 MN/m (round) and approx. 0.46 MN/m (triangular profile) smaller than the simulated values at 15,000 rpm. The authors assume that the gaps in the foil structure before mounting the shaft and the resulting preload in the bearing make a major contribution to this. This preload acts as a spring parallel to the bumps and softens the bearing. With larger loads, as in the red curve, the relative error is reduced because the additional force is only absorbed by the bumps. The curves with the greater load also show a declining behaviour (round: approx. 0.26 MN/m to approx. 0.18 MN/m), as can also be observed in the simulation (round: approx. 0.4 MN/m to approx. 0.3 MN/m). However, since the curves overlap only slightly, a direct comparison is not meaningful. As already discussed, the preload can shift the lift-off speed. For an ideally manufactured bearing, a lift-off at approx. 2600 rpm (round) and at approx. 8000 rpm (triangular profile) is calculated in the simulation. It is assumed that the bearing is completely lifted off with a minimum lubrication gap of 5 µm (static load: 5 N) [25]. In contrast, the tests (Figure 9) showed a lift-off at approx. 8500 rpm (round) and approx. 10,000 rpm to 10,500 rpm (triangular profile) for the same load range (blue and green curve). The difference is thus smaller, but still clearly noticeable with 1500 rpm to 2000 rpm. The final comparison is made between the simulation and the experiment on the basis of the frictional torque (Figure 12). In the simulation [25], solid friction is not taken into account. The frictional torques are thus only related to aerodynamic friction and are therefore at very small values of about 0.001 Nm (15,000 rpm). This is an order of magnitude smaller than in Figure 9. For this reason, only the ratio of the frictional torques of the triangular profile and the round shape is shown in Figure 12. The triangular profile bearing shows an increase by a factor of about 1.7 in the measurement series in the range of 5 N (between the blue and the green curve at 15,000 rpm). This is very similar to the factor of 1.45 from the simulations. The increase in load (red curve) significantly increases the difference between the two bearing shapes to a factor of approx. 2.4. Despite the smaller bearing clearance, the change between the bearing sleeves seems to cause a greater difference in the frictional torque in the experiment than in the simulation.

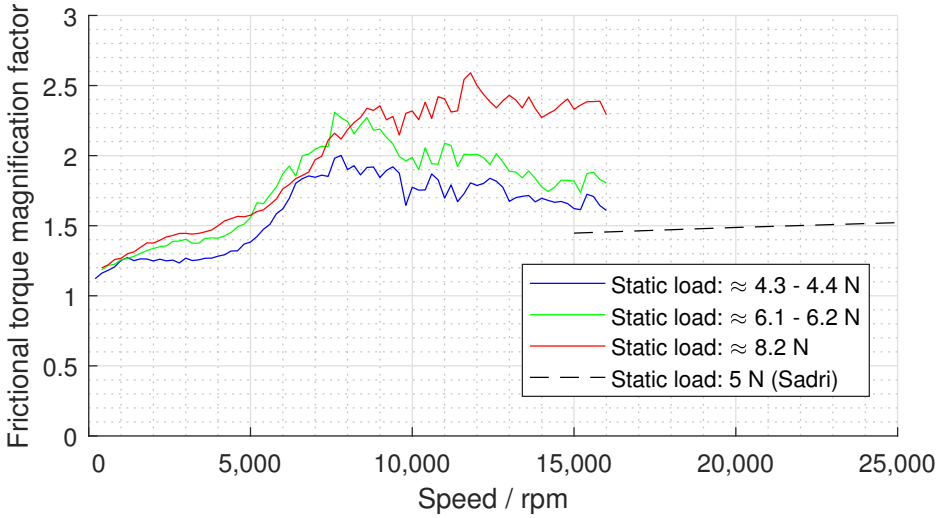

Figure 12. Calculated friction torque magnification factor between the two bearings from Figure 9 and from the results of Sadri [25].

5. Conclusions

Foil bearings seem to be ideal for use in air compressors for fuel cell vehicles due to their low friction, low maintenance requirement and small size. However, the many

start–stop cycles are particularly critical in this area. For this reason, this work contributes to the research of switchable bearing designs to improve the lift-off area in terms of friction and wear. First, the production of the bearing is described on the basis of methods from the literature. This reveals both problems in the measurement of the foil structure and a large scattering of the production deviations. The first consequence for the investigations is thus the reuse of the same foils in all tests. The experimental results show clear differences between the two initial shapes, round and triangular profile. The triangular profile bearing is associated with greater stiffness, greater frictional torques and a greater lift-off speed. The triangular profile bearing also seems to cause greater wear. The comparison with the literature confirms the observed characteristics. Finally, this paper discusses the transfer of the experimental results of the two rigid bearing configurations to the already simulated results of the prototype. Overall, the results confirm that the prototype can bring a clearly visible improvement by shifting in the starting range from a triangular profile to a round shape. The deviations found are probably due to manufacturing errors, such as the gap without a shaft mounted. For further work, the use of larger static loads is therefore being considered.

Furthermore, this work presents an improvement of the test method and the test rig. Particularly with small frictional torques, results from the literature indicate an insufficient consideration of offsets. Due to its new design, the test rig also improves the repeatability and the decoupling of load application and torque measurement. In addition, the presented test rig also allows the measurement of the displacements and the forces in both main axes.

Author Contributions: Investigation, H.S.; test rig design, H.S. and J.-H.S.; writing—original draft preparation, H.S.;writing—review and editing, M.S. and J.-H.S.; supervision, M.S.; project administration, M.S. All authors have read and agreed to the published version of the manuscript.

Funding: The authors gratefully acknowledge the financial support of the research work on this paper by the German Research Foundation (DFG) in the project "shape-variable film bearings" (280508116).

Institutional Review Board Statement: Not applicable.

Informed Consent Statement: Not applicable.

Data Availability Statement: Data is contained within the article.

Acknowledgments: We acknowledge support by the German Research Foundation and the Open Access Publication Funds of Technische Universität Braunschweig.

Conflicts of Interest: The authors declare no conflict of interest.

References

1. LI, W.; Feng, G. Design and Experimental Study of Centrifugal Compressor in Fuel Cell Vehicle. *Mechanics* **2021**, *27*, 52–61. [CrossRef]
2. Branagan, M.; Griffin, D.; Goyne, C.; Untaroiu, A. Compliant Gas Foil Bearings and Analysis Tools. *J. Eng. Gas Turbines Power* **2016**, *138*, 054001. [CrossRef]
3. Agrawal, G.L. Foil Air/Gas Bearing Technology—An Overview. In Proceedings of the ASME 1997 International Gas Turbine and Aeroengine Congress and Exhibition, Orlando, FL, USA, 2–5 June 1997; Volume 1, p. V001T04A006. [CrossRef]
4. Heshmat, H.; Walton, J.F.; Corte, C.D.; Valco, M. Oil-free turbocharger demonstration paves way to gas turbine engine applications. In Proceedings of the Turbo Expo: Power for Land, Sea, and Air, Munich, Germany, 8–11 May 2000; Volume 78545, p. V001T04A008.
5. Walton, J.F.; Tomaszewski, M.J.; Heshmat, C.A.; Heshmat, H. On the development of an oil-free electric turbocharger for fuel cells. In Proceedings of the Turbo Expo: Power for Land, Sea, and Air, Barcelona, Spain, 8–11 May 2006; Volume 42401, pp. 395–400.
6. Wale, G.D.; Mba, D. A Journal Bearing Test Rig With Reduced Uncertainty: Some Design Considerations. *J. Test. Eval.* **2007**, *35*, 1–30. [CrossRef]
7. DellaCorte, C. A New Foil Air Bearing Test Rig for Use to 700 °C and 70,000 rpm. *Tribol. Trans.* **1998**, *41*, 335–340. [CrossRef]
8. Howard, S.A. *A New High-Speed Oil-Free Turbine Engine Rotordynamic Simulator Test Rig*; NASA: Washington, DC, USA, 2007; p. 214489.
9. Rudloff, L.; Arghir, M.; Bonneau, O.; Matta, P. Experimental Analyses of a First Generation Foil Bearing: Startup Torque and Dynamic Coefficients. *J. Eng. Gas Turbines Power* **2011**, *133*, 092501. [CrossRef]

10. Ertas, B.H. Compliant Hybrid Journal Bearings Using Integral Wire Mesh Dampers. *J. Tribol.* **2009**, *131*, 022503. [CrossRef]
11. San Andrés, L.; Chirathadam, T.A. A Metal Mesh Foil Bearing and a Bump-Type Foil Bearing: Comparison of Performance for Two Similar Size Gas Bearings. *J. Eng. Gas Turbines Power* **2012**, *134*, 102501. [CrossRef]
12. Andrés, L.S.; Norsworthy, J. Measurement of drag torque, lift off speed and rotordynamic force coefficients in a shimmed BFB. *Kluwer Acad. Publ.* **2015**, *21*, 909–919. [CrossRef]
13. Sim, K.; Yong-Bok, L.; Ho Kim, T.; Lee, J. Rotordynamic Performance of Shimmed Gas Foil Bearings for Oil-Free Turbochargers. *J. Tribol.* **2012**, *134*, 031102. [CrossRef]
14. Sim, K.; Koo, B.; Sung Lee, J.; Ho Kim, T. Effects of Mechanical Preloads on the Rotordynamic Performance of a Rotor Supported on Three-Pad Gas Foil Journal Bearings. *J. Eng. Gas Turbines Power* **2014**, *136*, 122503. [CrossRef]
15. Mahner, M.; Bauer, M.; Lehn, A.; Schweizer, B. An experimental investigation on the influence of an assembly preload on the hysteresis, the drag torque, the lift-off speed and the thermal behavior of three-pad air foil journal bearings. *Tribol. Int.* **2019**, *137*, 113–126. [CrossRef]
16. Kim, D.; Zimbru, G. Start-Stop Characteristics and Thermal Behavior of a Large Hybrid Airfoil Bearing For Aero-Propulsion Applications. *J. Eng. Gas Turbines Power* **2012**, *134*, 032502. [CrossRef]
17. Zhang, G.; Xu, K.; Han, J.; Huang, Y.; Gong, W.; Guo, Y.; Huang, Z.; Luo, X.; Liang, B. Performance of textured foil journal bearing considering the influence of relative texture depth. *Proc. Inst. Mech. Eng. Part J. Eng. Tribol.* **2022**, *105*, 135065012110729. [CrossRef]
18. Ha, D.N.; Stolarski, T.A.; YOSHIMOTO, S. An aerodynamic bearing with adjustable geometry and self-lifting capacity. Part 1: Self-lift capacity by squeeze film. *Proc. Inst. Mech. Eng. Part J. Eng. Tribol.* **2005**, *219*, 33–39. [CrossRef]
19. Feng, K.; Guan, H.Q.; Zhao, Z.L.; Liu, T.Y. Active bump-type foil bearing with controllable mechanical preloads. *Tribol. Int.* **2018**, *120*, 187–202. [CrossRef]
20. Guan, H.Q.; Feng, K.; Cao, Y.L.; Huang, M.; Wu, Y.H.; Guo, Z.Y. Experimental and theoretical investigation of rotordynamic characteristics of a rigid rotor supported by an active bump-type foil bearing. *J. Sound Vib.* **2020**, *466*, 115049. [CrossRef]
21. Guan, H.; Feng, K.; Yu, K.; Sun, D.; Cao, Y. Real-Time Control of Rotor Vibrations With Active Bump-Type Foil Bearings. *IEEE Trans. Ind. Electron.* **2021**, *68*, 7412–7421. [CrossRef]
22. Park, J.; Sim, K. A Feasibility Study of Controllable Gas Foil Bearings With Piezoelectric Materials Via Rotordynamic Model Predictions. *J. Eng. Gas Turbines Power* **2019**, *141*, 021027. [CrossRef]
23. Sytin, A.V.; Shutin, D.V.; Polyakov, R.N. Applying Active Foil Bearings with Bimorph Piezoelectric Drives in Microturbines for Distributed Energy Systems. *Int. Conf. Ind. Eng.* **2021**, *57*, 446–455. [CrossRef]
24. Sadri, H.; Kyriazis, A.; Schlums, H.; Sinapius, M. On modeling the static shape control of an adaptive air foil bearing. *Smart Mater. Struct.* **2020**, *29*, 085043. [CrossRef]
25. Sadri, H. *Active Shape Control of the Lubricant Film Geometry in Adaptive Air Foil Bearings*; TU Braunschweig, Niedersächsisches Forschungszentrum für Luftfahrt: Braunschweig, Germany, 2020; pp. 49, 52–54, 56, 59, 124.
26. DellaCorte, C.; Radil, K.C.; Bruckner, R.J.; Howard, S.A. Design, Fabrication, and Performance of Open Source Generation I and II Compliant Hydrodynamic Gas Foil Bearings. *Tribol. Trans.* **2008**, *51*, 254–264. [CrossRef]
27. Shalash, K.; Schiffmann, J. On the manufacturing of compliant foil bearings. *J. Manuf. Process.* **2017**, *25*, 357–368. [CrossRef]
28. Żywica, G.; Bagiński, P.; Andrearczyk, A. A new method of manufacturing a foil bearing using tools made by the rapid prototyping technology. *CIRP J. Manuf. Sci. Technol.* **2020**, *31*, 514–524. [CrossRef]
29. Nielsen, B.B. *Combining Gas Bearing and Smart Material Technologies for Improved Machine Performance Theory and Experiment*; Technical University of Denmark: Lyngby, Denmark, 2017.